applied optics

Integrated optomechanical analyses and experimental verification for a thermal system of an aerial camera

Zhi-peng Xue,[1,2,*] Chun-xue Wang,[1] Yue Yu,[2,3] Peng-Peng Wang,[1] Hong-Yu Zhang,[1] Yuan-Yuan Sui,[2,3] Ming Li,[1,2] and Ze-yong Luo[1,2]

[1]Chang Guang Satellite Technology Company, 1299, Mingxi Road, BeiHu Science and Technology Development District, Changchun 130102, China
[2]Changchun Institute of Optics, Fine Mechanics and Physics, Chinese Academy of Sciences, 3888, Dong Nanhu Road, Changchun 130033, China
[3]University of Chinese Academy of Sciences, 19, A Yuquan Road, Beijing 100049, China
*Corresponding author: xuezhipengss1314@126.com

The thermal control system based on a combination of passive and active methods for a compact aerial camera used in the unmanned aerial vehicle system is studied. Integrated analysis and an experimental method are developed to ensure both low-power limit and high image quality of the camera. For rapid estimation of thermal behavior, we develop a thermal mathematic model based on a thermal network method that also offers an initial design reference for the active control system; then we develop a more complex integrated analysis method to analyze and optimize the thermal system, which allows us to get performance insights such as internal temperature gradient and airflow of the compact system. We also focus on analyzing the optical surface errors under thermal disturbance. Comparisons of interferometer test records and thermal-elastic simulation results are presented, and this comparison shows that the integrated optomechanical analysis method contributes to the success of optomechanical system design by ensuring thermal disturbance will not deform the optical surfaces beyond allowable limits. Finally, the design method is verified through a thermo-optic experiment.   © 2019 Optical Society of America

https://doi.org/10.1364/AO.58.006996

1. INTRODUCTION

Thermal management is a critical aspect of space and aerial optical system design to ensure performance requirements are met over the operational service environments. Generally, the thermal management of an aerial camera includes the use of passive and active control methods [1]. The passive thermal control method is the procedure to control the temperature of the component within the specified range by adjusting the paths of conduction and radiation; the active thermal control method is the procedure to control the temperature using mechanical mobile components or fluid, using electric energy from a heater, and changing the temperature [2].

The development of a thermal control system in an aerial camera typically involves a period of simulation and testing to ensure thermal requirements with relatively low power and mass [3]. The thermal mathematical modeling method often provides a rapid estimation of thermal behavior and an understanding of the parameters of the system. The traditional modeling method such as thermal network modeling is based on classic heat transfer theory, which divides the thermal

system into a number of finite subvolumes. Edeson *et al.* [4] constructed thermal mathematical models for an infrared camera using the software ESATAN, which uses a thermal network representation, and the analysis results of the model were taken as the temperature loads of the structural analysis. Another more accurate approach used in modeling the thermal system is using detailed finite element (FE) models. Liu *et al.* [5] established a FE thermal model for an aerial camera's primary optical system to simulate the temperature distribution.

More recent attention has focused on the optomechanical integrated analysis for high-performance optical systems. The benefit of performing integrated analyses is the ability to provide insight into the interdisciplinary design relationships of thermal and structural designs and their impact through a deterministic assessment of optical performance [6]. Johnston *et al.* [7] introduced an integrated structural-thermal-optical modeling method to predict the effect of thermal distortion on the optical performance of the James Webb Space Telescope. Bonin and McMaster [8] proposed a closed-loop optimization method using mechanical and optical analysis software;

the mechanical analysis software output is post-processed into Zernike polynomial coefficients. The modulation transfer function (MTF) is the basic and useful parameter to predict the image quality achieved by an imaging system [9,10]. Liu *et al.* [11] studied the temperature's effect on the MTF based on an integrated analysis process.

This paper is a contribution to extend thermal mathematic modeling method to the integrated optomechanical analysis process to a fast estimation of thermal behavior and provide a reliable initial design reference for the thermal control system. The objective of this work is to model the thermal system and develop an integrated optomechanical process for the performance analysis of the system. Another objective of this study is to investigate a comprehensive performance analysis, including thermal gradient, lens surface errors, airflow, MTF, etc., to be used to get the lowest heat power with satisfying optical performance. This paper proposes an analysis and experimental method, including thermal theoretical and integrated optomechanical analysis for the development of the thermal control system of an aerial camera. The focus holds on the following aspects:

(1) A detailed description of the calculation of the heating power based on the thermal mathematic model is given to show how thermal behavior can be effectively obtained before the integrated analysis.

(2) Describe how to access the effect of thermal behavior on optical surface accuracy and the parameter MTF based on the integrated optomechanical analysis; the interaction among thermal, structural, and optical analyses is also explored.

(3) Investigate the accuracy of the proposed analysis method by comparing the results obtained by the simulation and experiment.

In the next section, the design of the thermal system of the aerial camera is described. In Section 3, the thermal mathematic model is developed based on a network method to estimate the heat power needed by the thermal control system. Section 4 introduces an integrated optomechanical analysis for further investigating the temperature gradient and image quality of the camera. The calculation of MTF and optical surface errors is also presented in this section. Section 5 presents the thermo-optic experiment including the MTF test, followed by conclusions in Section 6.

2. THERMAL SYSTEM DESIGN

A. Introduction of the Camera

1. Composition of the Camera
The camera's size is 320L*252W*345H, and the weight is 12 kg, including focusing component, thermal control component, position and orientation system (POS), stable platform, and lens, as illustrated in Fig. 1(a). The lens component is shown in Fig. 1(b); the telecentric optical system includes 15 pieces of the lens in which the biggest and minimum diameters are 109 mm and 9.48 mm, respectively. The diameter of the quartz optical window is 170 mm and the axial length of the lens is 217 mm.

2. Thermal Environment
The aerial camera is assembled on the airframe of an unmanned aerial vehicle (UAV); the lower part of it is in direct contact with
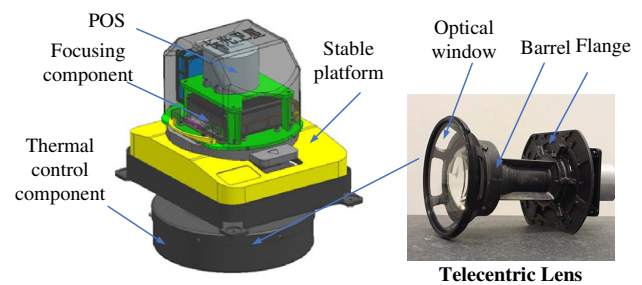

Fig. 1. Camera system.

outside air, as illustrated in Fig. 2. The flight attitude of the UAV is 400–1500 m, the cruising speed is 100 km/h, and the minimum operating temperature is −20°C. According to the optical system requirements, the ideal operating temperature of the lens is 15°C–30°C, the axial and radial temperature gradients should be less than 2°C, and the error of the MTF should be less than 10%.

3. Design Consideration
The optical system has high requirements for the processing and assembly accuracy of lenses and optical–mechanical structures. As illustrated in Fig. 3, each lens was placed in a cell and secured in place with a threaded retaining ring for holding lenses with good stability, and the preload torque was applied to the ring. In the lens mounting stage, an interferometer was used to measure the surface deformation of the optical elements to obtain an acceptable level between the mirror and mounting interfaces. However, it is difficult to track the surface accuracy of optical components after barrel assembly. Therefore, one of the objectives of this paper is to obtain the change in surface accuracy under thermal disturbance by simulation analysis and to analyze whether the surface deformation will have a significant impact on the performance of the optical system.

For the thermal control system of the compact camera studied in this paper, because of its narrow internal space, it is difficult to accurately measure the airflow, thermal distribution, and dynamic response of the structure by sensors in the process of prototype development and testing. Therefore, an integrated analysis method is needed to analyze the state of the system under disturbance conditions. The design of the thermal control system is a systematic project involving disciplines such as
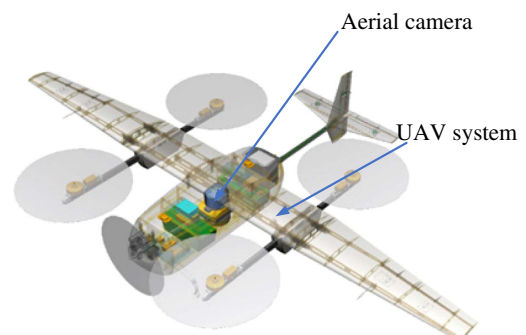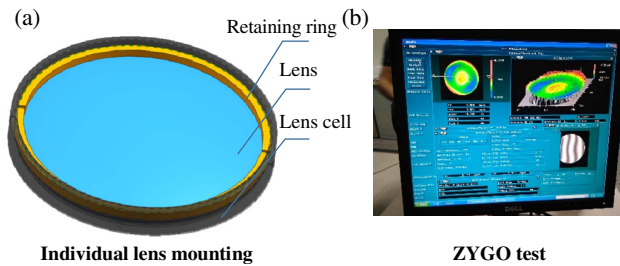

Fig. 2. UAV system.

Fig. 3.   Lens system.

thermal, mechanical, and optical. In designing a thermal system, it is especially important for the optical designer, and mechanical and thermal engineers to work closely together so that the low power and high image quality can be fully realized. Then a fast and efficient integrated analysis method will be needed, from mathematical calculation and simulation analysis to experimental verification of a complete process to analyze and optimize system performance.

B. Passive Thermal System Design

1. Thermal Housing Assembly Design

The thermal housing assembly design considers mainly the following:

(1) providing insulation between internal and external air of the thermal control system;

(2) reaching a relatively higher structure frequency using the minimum mass.

Multilayer sandwich composites were used in the lightweight design of the thermal housing assembly. The faces' material of the sandwich composites was glass fiber, and the core's material was foam. The comparison of the structural behavior of the housing assembly made by different materials is shown in Table 1. Apparently, the sandwich composite creates both lower mass and higher natural frequency.

2. Thermal Insulation System Design

The passive control methods as illustrated in Fig. 4 are as follows:

(1) a multilayer SiQ2 blanket is affixed to the inner face of the thermal housing assembly;

(2) the inner air is sealed against the outer environment to further reduce thermal conductivity;

(3) polyimide pads are used as the thermal interface;

(4) the interior surfaces of the lens and housing assembly are blackened to reduce stray light reflections within the system and to the uniform temperature distribution.

Table 1.   Structure Performance Comparison

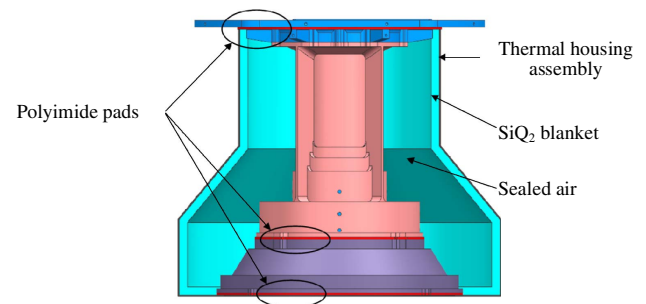| Material	7075AL	Sandwich Composites
Structure parameter	3 mm/1.5 mm	(a) ±45° glass fiber (0.115 mm)
		(b) 0°, 90°glass fiber (0.115 mm)
		(c) foam (2 mm)
		(d) ±45° glass fiber (0.115 mm)
Mass	555 g	350 g
Natural frequency	1257 Hz	1420 Hz

Fig. 4.   Passive control system.

The properties of insulation materials are shown in Table 2.

C. Active Thermal System Design

1. Heating Components

The heating component consists of a heater film, an aluminum bracket, and an axial fan, as shown in Fig. 5(a). The heat generated by the heater film is transferred by the conduction of the aluminum bracket quickly to the outlet of the axial fan, which blows the hot air to the target area.

Heating components A and B are placed, respectively, at the to and bottom of the thermal system. Component B blows hot air on the optical window directly, which not only improves the heat transfer efficiency but also avoids fogging and frosting of the window. However, there is no longer a need for indium tin oxide (ITO) film [12] to heat the optical window, which may influence the image quality of the optical system.

2. Control Strategy

A bang–bang controller is used to control heating components A and B, respectively, as shown in Fig. 5(b). The inputs of the controller are the values of temperature sensors, and the temperature is restricted between a lower and an upper bound. When the temperature drops to a predetermined low set point

Table 2.   Properties of Insulation Materials

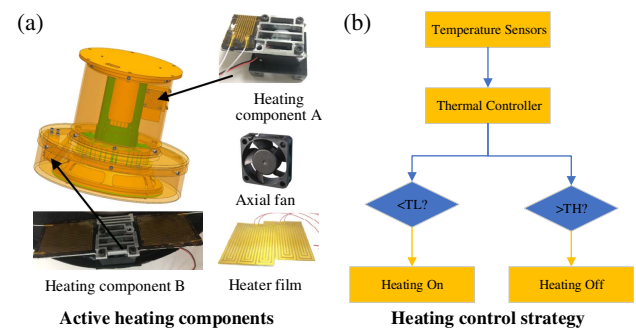| Properties	Density kg/m3	Heat Transfer W/(m · k)	Specific Heat J/(kg°C)
Polyimide pad	1430	0.35	1670–1750
SiQ2 blanket	130	0.018	502
Air	1.205	0.023	1005

Fig. 5.   Active control system.

(TL), the controller switches the heating system on; when the temperature reaches a pre-determined high set point (TH), the controller switches the heating system off. The temperature set points TH and TL are 22°C and 18°C, respectively.

3. THERMAL NETWORK MODELING

A. Thermal Network Theory

The thermal network modeling method is based on the classic heat transfer theory. The first step in thermal network modeling is subdividing the thermal system into a number of finite nodes. As illustrated in Fig. 6, each node represents two thermal network elements, temperature and capacitance. The temperature T assigned to a node represents the average mass temperature of the subvolume. The capacitance C assigned to a node is computed from the thermophysical properties of the subvolume material. The thermal resistance R is assigned to the sum of thermal conduction, convection, and radiation. The heat balance equation for all nodes of a thermal network can be written as

$$(cm)_i \frac{dT_i}{d\tau} = \sum_{i \neq j} D_{ij}(T_j - T_i) + \sum_{i \neq j} H_{ij}(T_j - T_i) + \sum_{i \neq j} R_{ij}(T_j^4 - T_i^4) + Q_{out}, \quad (1)$$

where, $D_{i,j}$, $H_{i,j}$, and $R_{i,j}$ are the thermal conduction, convection, and radiation coefficients, respectively, Q_{out} is the outer heat source, and $(cm)_i$ is the thermal capacity.

B. Thermal Mathematic Model

We choose the placement of the lumped node centers depending on the following factors:

(1) points where temperatures are desired;
(2) position where temperature distribution is expected;
(3) physical reasonableness;
(4) ease of computation.

We simplified the thermal system as 13 nodes, as illustrated in Fig. 7. According to the heat transfer relations between each node, the thermal network was designed as shown in Fig. 8.

The thermal resistances in the thermal network were then calculated based on the thermal principles [13], and the calculation of heat loss is as follows:

$$\varphi_i = \frac{\Delta T}{R_i}, \quad (2)$$

where φ_i is the heat loss, ΔT is the temperature difference, and R_i is the thermal resistance.
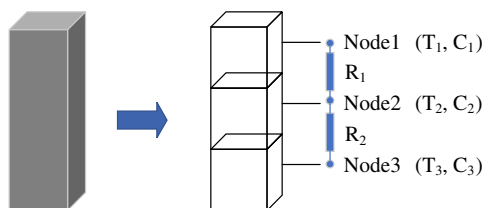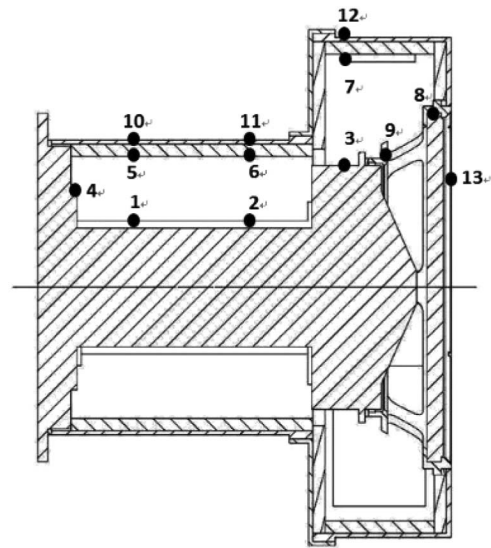

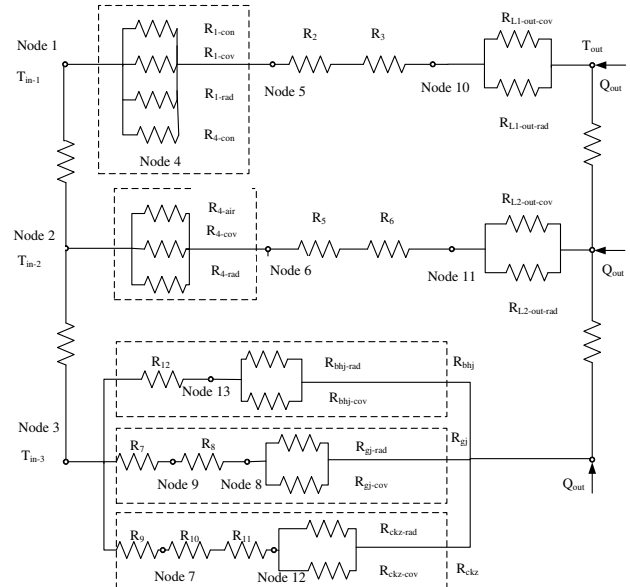**Fig. 6.** Nodalization.

Fig. 7. Nodalization of camera.

Fig. 8. Thermal network diagram of lens.

The main heat transfer roads are node 1-Q_{out}, node 2-Q_{out}, and node 3-Q_{out}, respectively. In Table 3, the thermal resistance and heat loss results under −20°C operational environment of the three heat transfer roads are presented. The calculation procedure of node 3-Q_{out} is presented in Appendix A.

Table 3. Thermal Network Results

Heat Transfer Road	Thermal Resistance	Heat Loss
Node 1-Q_{out} (φ_1)	9.5	4.21
Node 2-Q_{out} (φ_2)	15.5	2.58
Node 3-Q_{out} (φ_3)	1.1	36.3

The total heat loss of the camera is

$$\varphi = \varphi_1 + \varphi_2 + \varphi_3 = 43.09 \text{ W.} \tag{3}$$

4. INTEGRATED ANALYSIS METHOD

A. Image Quality Calculation

Image quality is critically important for aerial cameras used in photogrammetry. The MTF considers the response of the optical system to sinusoidal intensity distributions of varying spatial frequency [9]. The MTF curve is computed by plotting image contrast as a function of spatial frequency, which is a function of the spatial frequency f-number and is given as

$$\text{MTF}(f) = \frac{\pi}{4} \frac{|I_{\max} - I_{\min}|}{|I_{\max} + I_{\min}|}, \tag{4}$$

where $I_{\max}$ is the maximum intensity, and $I_{\min}$ is the minimum intensity of the image.

B. Optical Surface Error Calculation

In this paper, both thermal and structural analyses were solved by FE method aiming to calculate optical deformation due to thermal loads. The same FE model was used by thermal and structural analyses. The temperature of each node in the FE model was calculated by thermal analysis. Then the displacement of each node due to thermal conditions was calculated. As shown in Fig. 9, vector u_{p0} denotes the position of node P_0 of an optical element in the initial state, which moves to a new position u_{p1} due to the thermal loads. Based on the kinematics of infinitesimal deformation [14], the position of P_1 is

$$u_{p1} = u_{p0} + u_d, \tag{5}$$

where u_d is the displacement vector of node P_1.

The new position u_{p1} then was used by the fitting polynomial to create a new optical surface.

C. Process of Simulation

In order to predict optical behavior that can account for optical surface errors due to thermal loads, an optomechanical analysis was developed as shown in Fig. 10. To begin this process, a detailed FE model as shown in Fig. 11 was constructed in FE analysis software to calculate the thermal and structural response. Hexahedral and tetrahedral elements were used to construct the FE model, and the element number was 280000. The thermal analysis was performed first, and the initial heating powers were based on the theoretical analysis results in Section 3.A. Once the thermal analysis results met the thermal control requirements, a thermo-elastic analysis was performed
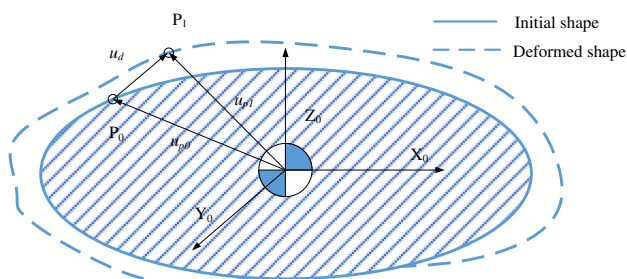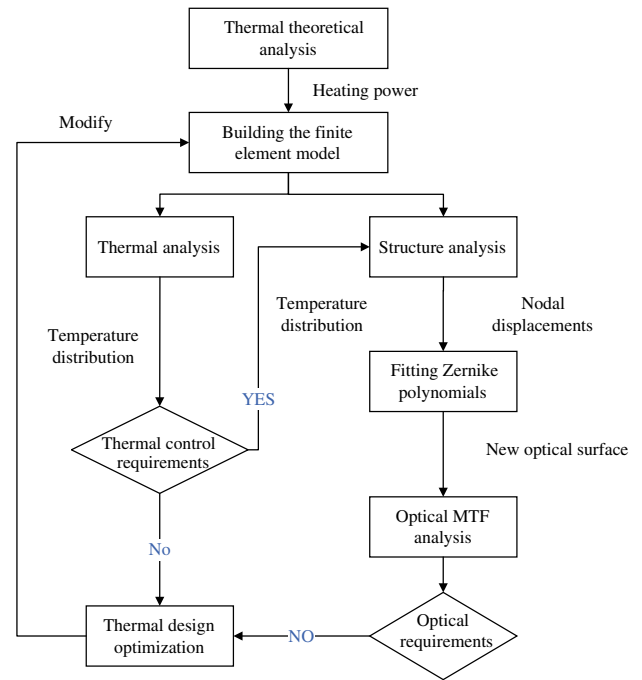

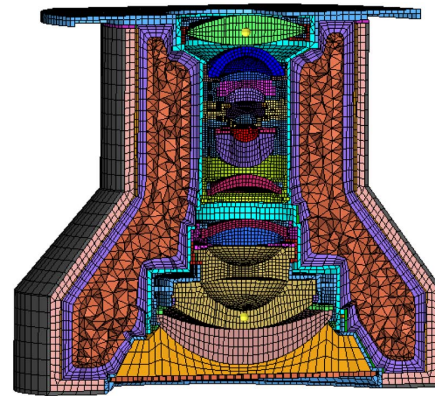**Fig. 10.** Optomechanical analysis interaction.

Fig. 11. Finite element model of thermal system.

to calculate the nodal displacements under the temperature fields calculated by the thermal analysis. Following the thermo-elastic analysis, we used Zernike polynomials to represent the optical surface deformations. Finally, an optical analysis was performed using optical software to compute the optical performance of the deformed optical system.

D. Simulation Results

1. Thermal Analysis

A thermal analysis was performed to compute the temperature distribution under the environment temperature –20°C. The steady-state temperature distributions are shown in Fig. 12; it is apparent in this figure that the resulting temperature distribution is an axial gradient with a slight radial variation. Table 4 presents the summary statistics for the temperature gradient of each lens. Both the radial and axial temperature

Fig. 9. Deformation of an optical element.
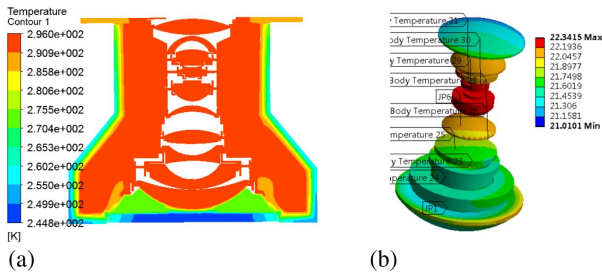
Fig. 12. Thermal analysis result: (a) lens system temperature distribution and (b) optical system temperature distribution.

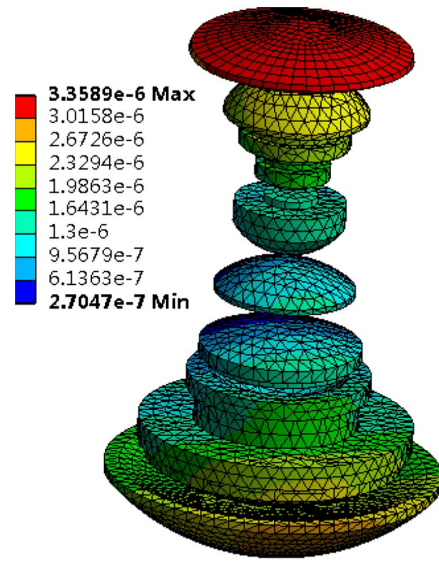**Table 4. Optical System Temperature Results (°C)**

Lens Num	Temperature	Gradient
1	21.2–22.1	0.9
2	21.3–21.6	0.3
3	21.5–21.9	0.4
4	21.6–22.0	0.4
5	21.6–22.0	0.4
6	22.0–22.3	0.3
7	22.2–22.3	0.1
8	22.3–22.3	0.03
9	22.2–22.2	0.03
10	22.2–22.3	0.1
11	22.1–22.2	0.1
12	22.1–22.2	0.1
13	22.0–22.2	0.2
14	21.8–22.2	0.4
15	21.2–21.8	0.6

Fig. 13. Thermo-elastic analysis result.

Table 5. PV and RMS of the Optical Deformation

Optical Surface	Test Records		Thermo-Elastic	
	PV	RMS	PV	RMS
Lens 2_upper	0.19	0.009	1.66	0.22
Lens 2_lower	0.11	0.012	1.01	0.13
Lens 7_upper	0.14	0.007	1.14	0.09
Lens 7_lower	0.25	0.006	1.29	0.17

differences are less than 2°C, which indicates that the simulation results meet thermal requirements.

2. Thermo-Elastic Analysis

A thermo-elastic analysis was performed to compute the deformations of the optical surfaces under the temperature field calculated by the thermal analysis. Figure 13 shows an overview of the resulting deformed shape. The displacements of the optical surfaces are between 0.3 µm and 3.3 µm.
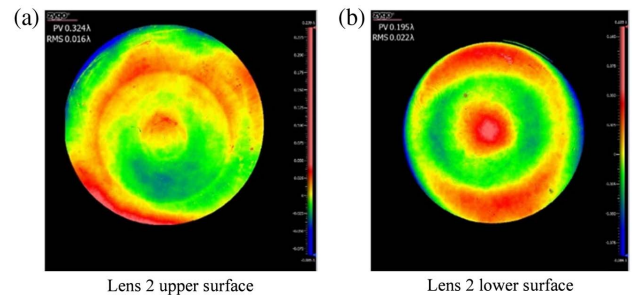
In the FE model, the preload torque and "glued contact" of the individual lens are modeled to ensure that the FE model can simulate the real physical state as much as possible. The interferometer test records of the optical surface after individual lens mounting and the thermo-elastic simulation results of lenses 2 and 7 are presented in Table 5. It is apparent from this table that the peak-to-valley (PV) values of the optical deformation changed greatly under the condition of thermal disturbance, while the root-mean-square (RMS) values changed relatively little. These are mainly because the circular contact area between the retaining ring and the lens produced large deformations, which results in a larger PV value. In other places, the structural glue as the medium of the cell and optical element effectively absorbs the stress caused by thermal deformation, so that the overall deformation accuracy of the mirror is very small. As shown in Fig. 14, these results also indicate that the metal-to-glass interfaces of individual lens mounting were

Lens 2 upper surface   Lens 2 lower surface

Fig. 14. Interferometer test record of lens 2.

designed successfully by ensuring that thermal disturbance does not deform the optical surfaces beyond allowable limits. However, further thermo-optical analysis is needed to determine whether the optical surface deformation will affect image quality.

3. Thermo-Optic Analysis

The results of the thermo-elastic analysis were post-processed by Zernike polynomial fitting [15]. Then the data were transferred to the optical software, and an optical analysis was performed to compute the optical performance of the newly created optical system. The MTF of the optical system is illustrated in Fig. 15. The average MTF at Nyquist frequency 91 lp/mm of the optical system decreases from 0.42 to 0.39.
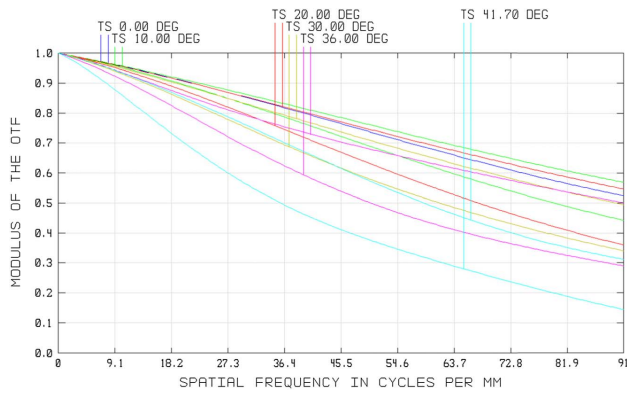
Fig. 15. MTF result.

With the impact of the thermal loads, the MTF of the optical system decreased by 7%.

4. Optimum Design

The method of the thermal network provides a very good initial reference for the position and power of active heating. However, due to the different complexity of the model, the active thermal control system was further optimized in the process of integrated simulation analysis. The geometry of the thermal control system belongs to a compact inverted T-shaped hollow structure. To avoid temperature gradient caused by active heating, one of the key points of integrated analysis is to optimize the position, outlet direction, and parameters of the fans in the upper and lower regions, so as to ensure uniform heat transmission through the movement of internal air.

In the process of optimization design, the internal airflow states under different outlet directions and wind forces were compared, and the temperature distribution under these conditions was further analyzed. As illustrated in Fig. 16(a), the method of vertical airflow needs more fans to ensure that the internal temperature meets requirements, and the optical window's temperature was difficult in meeting the requirements. Figure 16(b) shows the situation of using a circumferential airflow method with insufficient wind power; the airflow did not circulate well inside to ensure a good temperature gradient. After several iterations, the final design was obtained, as shown in Fig. 16(c). The average airflow rate is about 2 m/s, and the forced convection coefficient is around 40 W/(m2k). The upper fan contributes to reduce the temperature gradient of the upper area. Since the optical window is the location with the greatest heat loss, the lower fan blows the heat to the optical
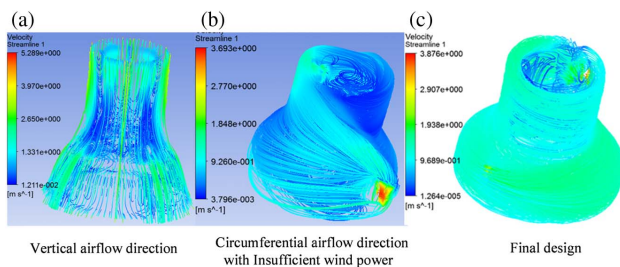

Fig. 16. Internal airflow design.

window directly and drives the lower airflow. It can also prevent fogging and frosting of the optical window.

After determining the design of the fans, the design of heating power becomes simple. Only a few iterations are needed. By adjusting the power of the two main heating positions, the minimum power that meets the requirements of temperature and gradient can be obtained.

5. THERMO-OPTIC EXPERIMENT

A. Introduction of Experiment Design

1. Experimental Setup

To verify the analysis method proposed in this paper, a thermo-optic experiment was set up. The frequency generation method was used to test the MTF of the camera [16]. An object consisting of a pattern having the Nyquist frequency was imaged by the camera under test, and the contrast of the image was measured directly. As shown in Fig. 17, the camera was placed in the environmental test chamber, and a test pattern was placed at the focal plane of the parallel light pipe. For the purpose of temperature measurement, eight temperature sensors were placed in the lens barrel's upper, middle, and bottom areas, respectively, as illustrated in Fig. 18.

2. Test Process

As illustrated in Fig. 19, the test process under the operational environment temperature is as follows:

Step ① Keeping the environment temperature at 20°C and measuring MTF, then switching the thermal control system on;
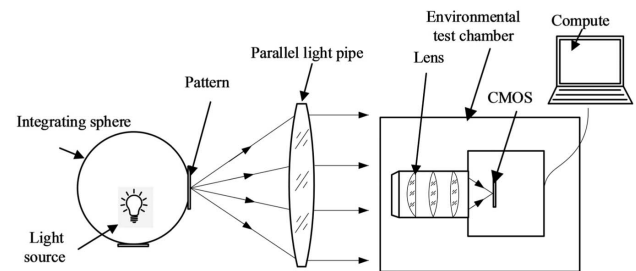

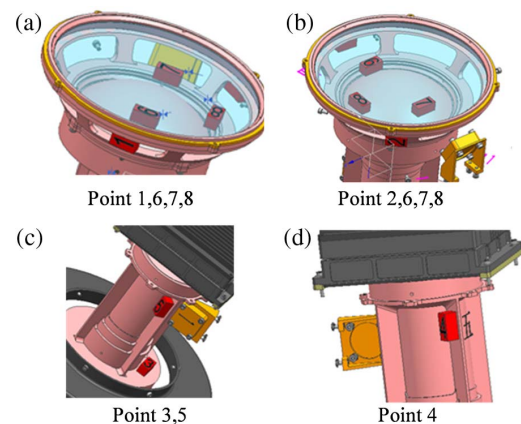**Fig. 17.** Experimental setup for MTF measurements.

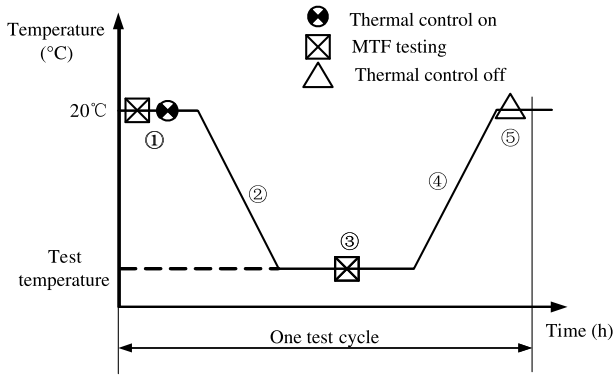**Fig. 18.** Position of temperature sensors.

Fig. 19. Test cycle diagram.

Step ② Cooling the camera to −20°C at a constant rate;
Step ③ Keeping the test temperature for 2 h and measuring MTF; for the purpose of heat loss measurement, electricity statistics of the heating system were also performed;
Step ④ Heating the camera to 20°C at a constant rate;
Step ⑤ Switching the thermal control system off.

3. Test Results

Figure 20 shows the experimental data measured by the eight sensors at −20°C environment temperature. It is apparent in this figure that the temperature of lenses was controlled between 19.5°C and 23°C. The temperature gradients between the eight measuring points are less than 2°C.

For the purpose of further thermal behavior analysis, the axial and radial temperature gradients of the lens are given by

$$T_{L\text{-axial}} = |(T_{p1} + T_{p2} + T_{p6} + T_{p7} + T_{p8})/5$$
$$- (T_{p3} + T_{p4} + T_{p5})/3|, \quad (6)$$

$$T_{L\text{-radial}} = \max(|T_{p1} - T_{p2}|, |T_{p4} - T_5|), \quad (7)$$

where $T_{p1} - T_{p8}$ denote the average temperature of the measuring sensors 1–8, respectively.

The average and gradient temperatures of the optical window are given by
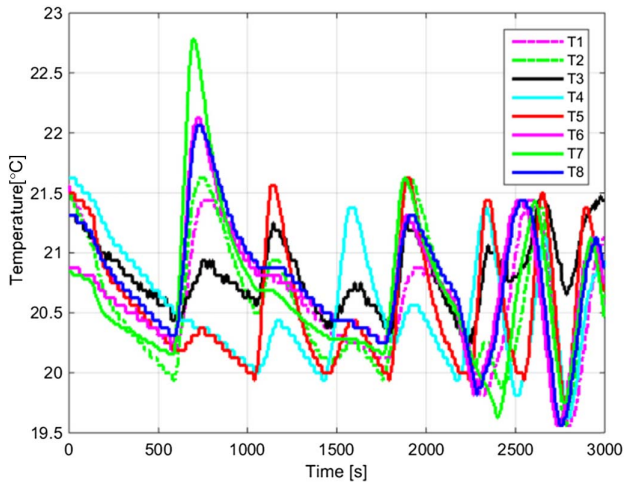
$$T_{W\text{-aver}} = (T_{p6} + T_{p7} + T_{p8})/3, \quad (8)$$

$$T_{W\text{-grad}} = \max(|T_{p6} - T_{pa}|, |T_{p7} - T_{pa}|, |T_{p8} - T_{pa}|). \quad (9)$$

The average temperature of the lens is written as

$$T_{L\text{-aver}} = (T_{p1} + T_{p2} + T_{p3} + T_{p4} + T_{p5})/5. \quad (10)$$

Table 6 presents the summary statistics for thermal behaviors of the camera under different experimental temperatures. It is apparent from this table that the average and gradient temperatures of the lens meet thermal requirements. The MTF experimental data of the camera system are shown in Table 7. Since the MTF of the COMS sensor is about 0.6 at the Nyquist frequency, the MTF of the camera system is about 60% of the lens' MTF. The variation of the system MTF under different experimental temperatures was very small, which was caused mainly by measurement errors.

In order to identify the accuracy of the proposed method, the heat powers obtained by the mathematic model, integrated analysis, and experiment are presented in Table 8. In summary, these results show that the thermal math model offered a rapid estimation with acceptable accuracy in the conceptual design stage, then the heat powers were modified during the integrated analysis. These differences were caused by a variety of factors, such as the detailed level of the analysis model, the parameters difference between the model and actual device, and the error caused by the instrument.

Based on the theoretical analysis, integrated simulation analysis, and thermal optics experiment of the thermal control system, we optimize and improve the thermal control system, and find the lowest power that can ensure the performance of the optical imaging system under the limit operating temperature. The optical–mechanical–thermal integrated simulation analysis enables us to evaluate the parameters of the internal

Table 6. Temperature Results (°C)

Test Temperature	$T_{L\text{-aver}}$	$T_{L\text{-axial}}$	$T_{L\text{-radial}}$	$T_{W\text{-aver}}$	$T_{W\text{-grad}}$
0	20	0.8	0.2	20.5	0.1
−10	20.5	0.9	0.4	19	0.3
−20	20.4	1.2	0.5	18.5	0.5

Table 7. Measuring Results of MTF

Test Temperature	20°C	0°C	−10°C	−20°C
MTF	0.239	0.229	0.246	0.231
MTF error	—	4.18%	2.92%	3.34%
Heating power (W)	—	27.4	36.4	51.3

Table 8. Comparison of Heat Loss

Test Temperature	Experiment	Integrated Analysis	Mathematic Model
Heating power (W)	51.3	48	43.09
Error	—	6.4%	16.1%

Fig. 20. Test records of eight temperature sensors.

system such as airflow, temperature, and structural response under disturbance conditions. These are especially important for the study of the performance of compact imaging systems. On the other hand, based on the comparison of experimental test results and simulation results, the model is continuously optimized, so that the model can predict the performance more and more accurately.

6. CONCLUSION

In this investigation, a general and systematic methodology has been presented to assess the thermal control system's performance considering both thermal and optical requirements. The interaction among thermal, structural, and optical analyses was investigated. In general, therefore, it seems that the thermal math model was effective, offering rapid estimation of the thermal behavior of the system. The results of this study indicate that the integrated optomechanical analysis method has achieved accurate solutions for estimating the thermal and optical behavior of the system. Based on the results of this study, the following main conclusions can be drawn:

(1) The key step in the integrated analysis process is that the data processing includes interpolation and fitting to provide efficient means of data transfer between different analysis software.

(2) Experimental/simulation comparison proves an acceptable accuracy of the developed model and simulation. A more accurate mathematic model or FE model can be obtained by using the thermal parameters measured from thermal experiment.

(3) A limitation of this study is that the rigid-body errors and higher-order elastic deformation were not separated in the calculation of the optical surface errors. Further studies are needed to assess the image quality effects of the rigid-body errors, including decenter, despace, and tilt [17] due to the thermal loads.

Generally speaking, we observe that the integrated analysis method proposed in this paper effectively offers good potential to be applied to other optomechanical systems to meet the requirements of lower-power and high MTF.

APPENDIX A: HEAT LOSS CALCULATION OF NODE 3-Q_{out}

The thermal network diagram of node 3-Q_{out} is shown in Fig. 8, where R_7, R_8, R_9, R_{10}, R_{11}, and R_{12} are the thermal conduction resistances of optical windows' polyimide insulation, lens structure, SiQ$_2$ blanket, thermal housing assembly, optical window, and inner air, respectively. $R_{bhj-cov}$ and $R_{bhj-rad}$ are the resistances of the optical window of convection and radiation heat transfer, respectively. $R_{ckz-cov}$ and $R_{ckz-rad}$ are the resistances of the bottom of the thermal housing assembly of convection and radiation heat transfer, respectively. R_{gj-cov} and R_{gj-rad} are the convection and radiation resistances of the bottom of the lens structure, respectively. The thermal resistances are calculated based on thermal principles [12], and the results are shown in Table 9.

Table 9. Thermal Resistance Results

Thermal Resistance	R_7	R_8	R_9	R_{10}	R_{11}	R_{12}
Results	12.37	0.19	3.52	16.53	0.011	0.271
Thermal resistance	$R_{bhj-cov}$	$R_{bhj-rad}$	$R_{ckz-cov}$	$R_{ckz-rad}$	R_{gj-cov}	R_{gj-rad}
Results	0.97	1069	1.01	112.1	7.6	841

The thermal resistance of each part is calculated as follows:

$$R_{bhj} = R_{12} + \cfrac{1}{\frac{1}{R_{bhj-cov}} + \frac{1}{R_{bhj-rad}}} = 1.24, \qquad \text{(A1)}$$

$$R_{ckz} = R_9 + R_{10} + R_{11} + \cfrac{1}{\frac{1}{R_{ckz-cov}} + \frac{1}{R_{ckz-rad}}} = 21.06, \qquad \text{(A2)}$$

$$R_{gj} = R_7 + R_8 + \cfrac{1}{\frac{1}{R_{gj-cov}} + \frac{1}{R_{gj-rad}}} = 20.1, \qquad \text{(A3)}$$

$$R_{N3} = \cfrac{1}{\frac{1}{R_{bhj}} + \frac{1}{R_{ckz}} + \frac{1}{R_{gj}}} = 1.1, \qquad \text{(A4)}$$

where R_{bhj} is the thermal resistance of the optical window component, R_{ckz} is the thermal resistance of the thermal housing assembly, R_{gj} is the thermal resistance of lens structure, and R_{N3} is the thermal resistance of node 3-Q_{out}.

The heat loss under –20°C environment temperature of the node 3-Q_{out} is as follows:

$$\varphi_3 = \frac{\Delta T}{R_{N3}} = 36.3, \qquad \text{(A5)}$$

in which

$$\Delta T = T_{envi} - T_{tar}, \qquad \text{(A6)}$$

where $T_{envi} = $ –20°C, which is the environment temperature, and $T_{tar} = $ 20°C, which is the thermal control target temperature.

REFERENCES

1. T. Augustyn, "The KS-146A long range oblique photography (LOROP) camera system," Proc. SPIE **309**, 76–84 (1981).
2. D. Gilmore, *Spacecraft Thermal Control Handbook* (2002), Vol. **I**.
3. Y. Gao, B. Zhang, L. Chen, B. Xu, and G. Gu, "Thermal design and analysis of the high resolution MWIR/LWIR aerial camera," Optik **179**, 37–46 (2018).
4. R. L. Edeson, B. M. Shaughnessy, M. S. Whalley, K. Burke, and J. Lucas, "The mechanical and thermal design and analysis of the VISTA infrared camera," Proc. SPIE **5497**, 508–519 (2004).
5. L. Wei-Yi, D. Ya-Lin, W. Qing-Wen, J. Ji-Qiang, G. Liang, and W. Ling-Hua, "Thermal analysis and design of the aerial camera's primary optical system components," Appl. Therm. Eng. **38**, 40–47 (2012).
6. K. B. Doyle, V. L. Genberg, and G. J. Michels, *Integrated Optomechanical Analysis* (SPIE, 2002).
7. J. D. Johnston, J. M. Howard, G. E. Mosier, K. A. Parrish, M. A. McGinnis, A. M. Bluth, K. Kim, and K. Q. Ha, "Integrated modeling

activities for the James Webb Space Telescope: structural-thermal-optical analysis," Proc. SPIE **5487**, 600–611 (2004).

8. D. Bonin and B. McMaster, "Closed loop optimization of opto-mechanical structure via mechanical and optical analysis software," Proc. SPIE **6550**, 65500X (2007).

9. G. D. Boreman, *Modulation Transfer Function in Optical and Electro-Optical Systems* (SPIE, 2001).

10. O. Hadar, I. Dror, and N. S. Kopeika, "Image resolution limits resulting from mechanical vibrations. Part IV: real-time numerical calculation of optical transfer functions and experimental verification," Opt. Eng. **33**, 566–579 (1994).

11. W. Liu, H. Shen, Y. Xu, Y. Song, H. Li, J. Jia, and Y. Ding, "Developing a thermal control strategy with the method of integrated analysis and experimental verification," Optik **126**, 2378–2382 (2015).

12. J. Kang, H. Kim, K. S. Kim, S. K. Lee, S. Bae, and J. H. Ahn, "High-performance graphene-based transparent flexible heaters," Nano Lett. **11**, 5154–5158 (2011).

13. K&K Associates, *Thermal Network Modeling Handbook* (2000).

14. A. A. Shabana, "Flexible multibody dynamic: review of past and recent developments," Multibody Syst. Dyn. **1**, 189–222 (1997).

15. H. Lee, "Use of Zernike polynomials for efficient estimation of ortho-normal aberration coefficients over variable noncircular pupils," Opt. Lett. **35**, 2173–2175 (2010).

16. M. Wilcox, "How to measure MTF and other properties of lenses," Tech. Rep. (Optikos Corporation, 1999).

17. K. M. Schwertz and J. H. Burge, *Field Guide to Optomechanical Design and Analysis* (SPIE, 2012).